



Charge separation and dissipation in molecular wires under a light radiation

Hang Xie^{a,*}, Yu Zhang^b, Yanho Kwok^c, Wei E.I. Sha^d

^a Department of Physics, Chongqing University, Chongqing, 401331, PR China

^b Theoretical Division, Los Alamos National Laboratory, New Mexico, United States

^c Department of Chemistry, the University of Hong Kong, Hong Kong, China

^d College of Information Science & Electronic Engineering, Zhejiang University, Hangzhou, 310027, PR China

ABSTRACT

Photon-induced charge separation in nanowires or molecular wires had been studied in previous experiments and simulations. Most researches deal with the carrier diffusions with the classical phenomenological models, or the static energy level calculations by quantum mechanics. Here we give a dynamic quantum investigation on the charge separation and dissipation in molecule wires. The method is based on the time-dependent non-equilibrium Green's function theory. Polyacetylene chain and poly-phenylene are used as model systems under a light pulse with the energy larger than the band gap. The dynamic transition and the dissipation processes of the non-equilibrium carriers are studied in these open nano systems. With the bias potentials or impurity atoms, the complicated charge separation process is also observed and discussed. Our calculations show that the separation speed of the electron/hole-type wave packets ranges from about 0.2×10^6 m/s to 0.6×10^6 m/s, and it may be reduced by the Coulomb interaction and an intensive radiation; and the asymmetric carrier separations are found due to the different effective masses of electron/hole of the molecular wire.

1. Introduction

In the development of photovoltaic devices, some nanostructures such as graphene, silicon-nanowires, and 2D materials have attracted a lot of interest [1,2]. In these nanostructures, their energy band structures could be modulated by the chemical doping, geometric cutting or the strains existing in them [3–6]. Thus their power conversion efficiency (PCE) can be affected by these factors. To increase the PCE of these nanostructures, the charge separation is a very important factor. It may be realized in the p-i-n typed nanowires by different atom doping or bias potentials exerted on two regions. On the other hand, the strains in nanowires would change their band structures, which lead the spontaneous electron-hole separation in the real space [5].

Regarding the experimental aspect, recently the pump-probe technique in the ultrafast optics is used to directly analyze the transient charge separation process in silicon nanowires [6–8]. In the bending nanowires, the induced strain in them also increases the electron-hole recombination rate [6].

On the theoretical and computational aspect, the traditional drift-diffusion equation describes the carries movement under the light illumination in a large scale [7–11]. In this classical theory, some parameters (e.g. carrier recombination rate and life time) are obtained from some phenomenological models such as the Shockley-Read-Hall model

[9]. In nano-scale, we have to describe these phenomena by quantum mechanics. For example, the Bethe-Sapltter equation (BSE) is often employed for the exciton generation [12,13], in which the exciton wavefunction is expanded into the products of conduction (electron) and the valence (hole) wavefunctions. On the calculation aspects, nowadays many first-principles calculations, such as the density functional theory (DFT), are employed for studying the energy band of nanowires under light illumination [13–16]. Combined with the non-equilibrium Green's function (NEGF) theory, DFT calculations are also employed for the nano-structured photovoltaics [17–19]. For molecular wires, the charge transfer and separation are also investigated by (TD) DFT or other quantum chemistry calculations [20,21].

Among these works, the calculation for the dynamic charge separation process is still unexplored in the nano-scale devices, based on the ballistic quantum calculation. Recently we have developed a set of hierarchical equations of motion method (HEOM) to study the time-dependent quantum transport [22–25]. This method does not solve the Green's function directly, but it constructs dissipation matrices to account the non-equilibrium and open system conditions, which can constitute a close set of equation of motions together with the density matrix. It can easily deal with the large systems, even for the realistic systems with the DFT Hamiltonian [25]. This method may also be employed to study the nano structured photovoltaics when involving

* Corresponding author. Department of Physics, Chongqing University, Chongqing, 401331, PR China.
E-mail address: xiehangphy@cqu.edu.cn (H. Xie).

the electron-photon interaction.

In this paper we adopt this tool to investigate the transient electron-hole generation and separation in nanowires directly in time and space domain. In Sec. II we give a description for the models and the theory. Sec. III shows the results and discussions. We firstly use our theory to give a description for the quantum transition and dissipation process of the non-equilibrium carriers in the open systems under illumination. Then we find that the bias potential or the doping atoms in the molecular wires can induce the electron-hole separation with a laser radiation in the molecular wire. The dynamics pictures obtained by our method are much different from the traditional classical calculations, based on the spread nature of the electron/hole waves. In these molecular wires, we find that the wave-packet speed changes in different doping situations, Coulomb interaction, light intensities and band structures. For the doped system, the energy band calculation obtained from a first-principles model is employed to reconstruct an effective tight-binding Hamiltonian. In Sec. IV we conclude that our method is a good tool to study the charge separation and dissipation processes in the open nano structures.

2. Model and theory

2.1. Tight binding model and quantum transport schemes

In this paper we use the polyacetylene (PA) and poly-(p-phenylene) (PP) or doped PP as the research systems. For PA, due to the Peierls distortion [26], the polyacetylene has the alternative single and double bonds. The trans-form (Fig. 1(a)) is more thermodynamically stable than the cis-form. In our calculation, we use the nearest neighbor tight-

binding (TB) model for the carbon atoms with two hopping integral parameters ($t_1 = -2.7$ eV and $t_2 = -2.0$ eV) to represent the two types of bonds (Fig. 1(a)). For PP chains, we also only consider the carbon atoms in the nearest neighbor TB model with a single hopping integral ($t = -2.7$ eV) (Fig. 1(b)). For the doped PP chain (Fig. 1(c)), the on-site energies of the carbon (and the doped nitrogen and boron) atoms are changed properly to fit for the first-principles band results. The details are given in Sec. III. It is noted that in the light radiation, the geometry of these molecular wires will change, and the geometry change of molecular systems often leads important effects on the transport properties [27–29]. However, in this paper the laser pulse is very short, or the intensity of the continuous laser radiation is not very strong. Thus the geometry change is small which only leads a little modification to the hopping integrals. We neglect this radiation-induced geometry change in this work.

In the quantum transport calculation for the exciton generation and charge separation, we choose two schemes for the doping effect. In the first scheme we artificially adjust the on-site energy of each atom with the averaged potentials in the p-doped or n-doped regions (Fig. 1(d)). In the second scheme we change the on-site potentials for some atoms to represent the two types of doping (Fig. 1(e)). To investigate the dynamic charge separation, we set a laser pulse to radiate in the middle region of the PA/PP chain and then calculate the electron evolution in the open system by the method described below. Due to the computational limitation, the radiation region is set to be much smaller than the actual spot size of the laser beam. However, our calculation results show that such a small radiation region is enough to observe the charge separation process in the molecular wires.

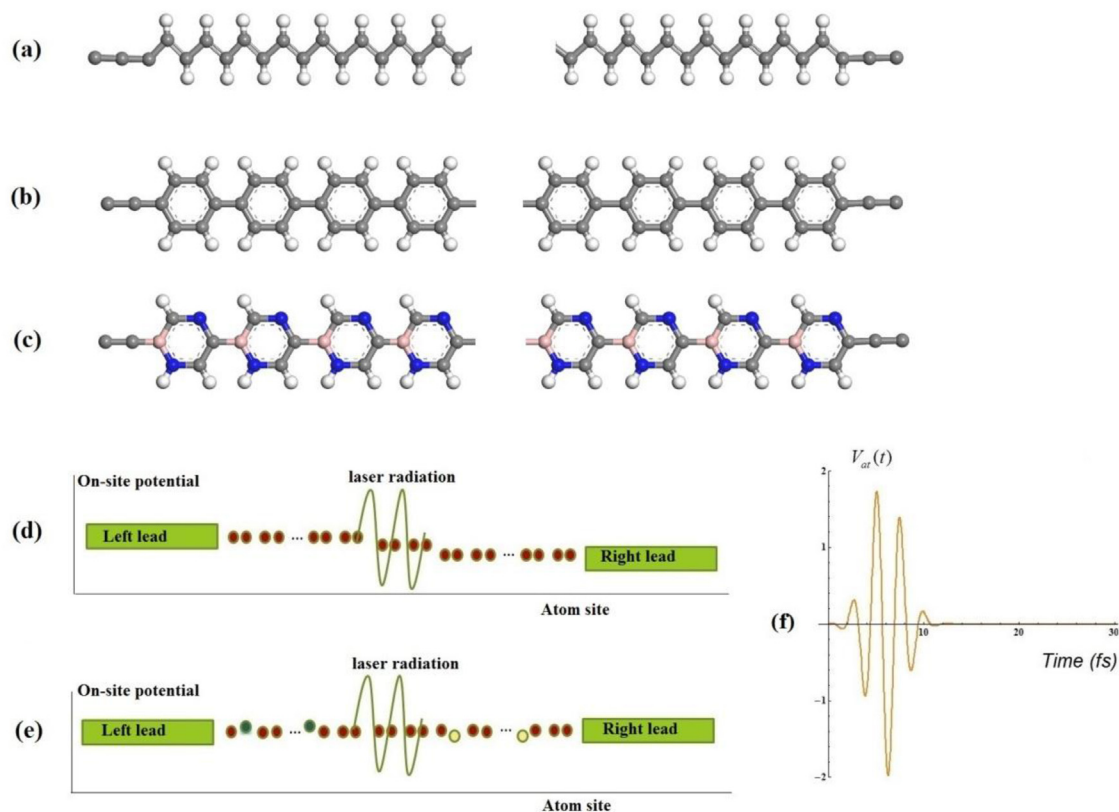


Fig. 1. (a) Atomic figure for the PA chain; (b) Atomic figure for the PP chain; (c) Atomic figure for PP chain doped with boron (pink) and nitrogen (blue) atoms; In (a)–(c), two carbon-atom chains sandwich the middle molecular wires for the WBL condition (see Sec.2.2 for details). (d) and (e) Schematic picture for the molecular wire system under a laser radiation with impurity atoms. The sine curves in the middle represent the laser beams radiated on the p-i-n junction of the molecular-wire systems. In (d) the impurity atoms are represented by two averaged bias potentials on both sides; while in (e) the impurities are represented by the single impurity atoms with positive or negative on-site potentials. (f) The time dependence of the laser pulse. (For interpretation of the references to color in this figure legend, the reader is referred to the Web version of this article.)

2.2. HEOM -WBL theory

In this study, we employ our developed HEOM theory [22,24] to solve the electron dynamics for the molecular wires. Due to the large size of the long molecular wire, we also utilize the wide-band-limit (WBL) approximation in the calculation. A brief introduction for this HEOM-WBL theory is given below.

In the quantum transport calculations, an open system is partitioned into three regions: the left lead (*L*), the device (*D*) and the right lead (*R*). The equation of motion for the density matrix of the device is

$$i\dot{\sigma}(t) = [\mathbf{h}_D(t), \sigma(t)] - \sum_{\alpha}^{N_k} [\varphi_{\alpha}(t) - \varphi_{\alpha}^{\dagger}(t)], \quad (1)$$

where $\sigma_D(t)$ and $\mathbf{h}_D(t)$ are the single-electron density matrix and Hamiltonian of the device. $\varphi_{\alpha}(t)$ is called the auxiliary density matrix, which corresponds to the dissipation effect from the leads. With the residue theory, the auxiliary density matrix can be written as [22]

$$\varphi_{\alpha}(t) = i \left(\sigma(t) - \frac{\mathbf{I}}{2} \right) \cdot \Lambda_{\alpha}^z + \sum_{k=1}^{N_k} \varphi_{\alpha,k}(t), \quad (2)$$

where $\varphi_{\alpha,k}(t)$ is defined as the discrete auxiliary density matrix. Its detailed expression can be found in other references [22,24]. The EOM of $\varphi_{\alpha,k}(t)$ is derived as

$$i\dot{\varphi}_{\alpha,k}(t) = \frac{2iR_k}{\beta} \Lambda_{\alpha}^z + [\mathbf{h}_D(t) - (\Delta_{\alpha}(t) + z_k/\beta)\mathbf{I} - i\Lambda] \cdot \varphi_{\alpha,k}(t), \quad (3)$$

where $\Delta_{\alpha}(t)$ is the bias potential of the lead α ; Λ_{α} is the linewidth function of the lead α with the definition $\Lambda_{\alpha} = -\text{Im}[\Sigma_{\alpha}^r(\varepsilon = 0)]$ and $\Lambda = \sum_{\alpha} \Lambda_{\alpha}$; \mathbf{I} is a unit matrix; z_k and R_k are the k th Padé pole and coefficient for the Padé expansion of the Fermi-Dirac function [22,24]

$$f_{\alpha}(\varepsilon) = \frac{1}{2} - \frac{1}{\beta} \sum_k^{N_k} \left[\frac{R_k}{\varepsilon - \Delta_{\alpha} - z_k/\beta} + \frac{R_k}{\varepsilon - \Delta_{\alpha} + z_k/\beta} \right] \quad (4)$$

with β being the inverse temperature. We see that Λ_{α} is related to the imaginary part of self-energy matrix at the zero energy, which is a constant for the WBL approximation. Eqs. (1)–(3) are the central equations for the HEOM-WBL theory.

The initial values of $\sigma(t)$ and $\varphi_{\alpha,k}(t)$ are obtained from the residue theorem with the following expressions [22]

$$\sigma(0) = \frac{1}{2}\mathbf{I} + \sum_{k=1}^{N_k} \text{Re} \left\{ \left(\frac{-2R_k}{\beta} \right) [(z_k/\beta)\mathbf{I} - \mathbf{h}_D(0) + i\Lambda^z]^{-1} \right\}, \quad (5)$$

$$\varphi_{\alpha,k}(0) = \frac{2iR_k}{\beta} [(\Delta_{\alpha}(0) + z_k/\beta)\mathbf{I} - \mathbf{h}_D(0) + i\Lambda^z]^{-1} \cdot \Lambda_{\alpha}^z. \quad (6)$$

After calculating the initial state of the system, some iteration methods (such as 4th-order Runge-Kutta scheme) are to be used to investigate the dynamic process of these quantum open system.

2.3. Coulomb interaction

In our systems, electron is excited by the light to the conduction band and hole forms in the valence band. In the real space, the fluctuated charges on each atom site induced by the radiation also have the additional Coulomb interactions with each other. These fluctuated charges lead to a re-distribution of the electric potential in the system, besides the original band structures without any external field. In the density-functional-based tight-binding (DFTB) model, the Coulomb interaction is involved in the following formula [30–32]

$$E = \sum_i^{\text{occ}} \langle \Psi_i | H_0 | \Psi_i \rangle + \frac{1}{2} \sum_{\alpha, \beta}^N \gamma_{\alpha\beta} \Delta q_{\alpha} \Delta q_{\beta}, \quad (7)$$

where $\Delta q_{\alpha} = q_{\alpha} - q_{\alpha}^0$, is the Mulliken charge difference between the charged and neutral atom α ; $\gamma_{\alpha\beta}$ is the quantity to measure the electron-

electron interaction. The first term is the band energy without any charge fluctuation, including the Coulomb energy (Hartree term) generated by q_{α}^0 . In the framework of DFTB theory, the exchange and correlation energies are considered as a functional term in H_0 . $\gamma_{\alpha\beta}$ is a function of the distance between atom α and β , which decays as $1/|\mathbf{R}_{\alpha} - \mathbf{R}_{\beta}|$ at large distances between two atoms and behaves as the Hubbard-like term $\gamma_{\alpha\alpha} = U_{\alpha}$ when $\mathbf{R}_{\alpha} = \mathbf{R}_{\beta}$ in the on-site case [30]. The Hubbard parameter U_{α} is fitted from the DFT calculation for the spin unpolarized electron systems [31]. By using the variational principle to Eq. (7), the Hamiltonian is obtained for the Coulomb-involved system [30,32]. In fact, DFTB is a second-order expansion of Kohn-Sham total energy with respect to charge fluctuations (Δq_{α}).

In our work, we use a simplified Hamiltonian to include the Coulomb interaction

$$\mathbf{h}_D = \sum_{\langle i,j \rangle} t_{i,j}(t) c_i^{\dagger} c_j + \sum_i c_i^{\dagger} c_i \sum_j \gamma_{i,j} (\sigma_j(t) - \sigma_j(0)) \quad (8)$$

The first term is the common TB Hamiltonian without the Coulomb interaction; $\langle i,j \rangle$ means only the nearest neighbor hopping integrals are considered; $t_{i,j}(t)$ is time-dependent for the EM radiation field, as will be presented below. The second term refers to the Coulomb potential exerted on the atom-site i , summed by all the atoms of the sites j with the Coulomb factor $\gamma_{i,j}$ [30]. $\sigma_j(t)$ and $\sigma_j(0)$ are the electron densities of the atom-site j at the time t and 0 respectively.

We note that this consideration is equivalent to the Poisson equation which is often used in the quantum transport calculations.

2.4. Electron-photon interaction

In our calculations, the electron-photon interaction (EPI) Hamiltonian is utilized as [33,34]

$$H_{i,j}^0 e^{i \int_{\mathbf{r}_i}^{\mathbf{r}_j} \frac{e}{\hbar} \mathbf{A} d\mathbf{r}} = H_{i,j}^0 e^{i \frac{e}{\hbar} \mathbf{A}(\mathbf{R}_i - \mathbf{R}_j)} \quad (9)$$

where \mathbf{A} is the vector potential along the molecular wire direction. Actually $\mathbf{A}(\mathbf{r})$ is spatial dependent, and the formula above is only valid in the long-wave limit. However, in our situation the EM wavelength is much longer than the molecular wire, so this approximation always holds.

We see that the electromagnetic (EM) field causes an additional phase factor on the Hamiltonian. This exponent factor is called the Peierls phase factor φ_p . For the PA chain, only the nearest-neighbor hopping terms are non-zero, and we assume $|\mathbf{R}_i - \mathbf{R}_{i\pm 1}| = a$ in the TB model, where a is the average distance of the carbon chain. So we have $\varphi_p = \frac{e}{\hbar} Aa = \varphi_0 \cos(\omega t)$. With the Coulomb gauge, \mathbf{A} is related to the electric field \mathbf{E} : $\mathbf{A} = \mathbf{E}/\omega$. Although the electric field here is a non-conservative field, we still may define an equivalent electric potential (EEP) V_m , which is related to the electric field by: $\mathbf{E} = V_m/(Na)\mathbf{e}_E$, where N is the number of atoms along the molecular wire, \mathbf{e}_E is the vector unit of \mathbf{E} . Then we have

$$\varphi_0 = \frac{e}{\hbar} \left(\frac{1}{\omega} \frac{aV_m}{Na} \right) = \frac{e}{\hbar} \left(\frac{aV_m}{Na} \right) \left(\frac{\hbar}{e\omega_V} \right) = \frac{V_m}{N\omega_V}, \quad (10)$$

where $\omega = \omega_V \frac{e}{\hbar}$, ω_V is the dimensionless angular frequency.

3. Results and discussions

3.1. Electron evolution in PA systems under a uniform radiation

Firstly, we calculate for the occupation number changes of the molecular orbitals in a finite PA chain under a uniform EM radiation. For such a finite molecular chain, we obtain the eigenstates ϕ_n and the density matrix σ from the eigenvalue calculation [35]

$$\mathbf{H}_0 \phi_n = E_n \phi_n, \quad (11)$$

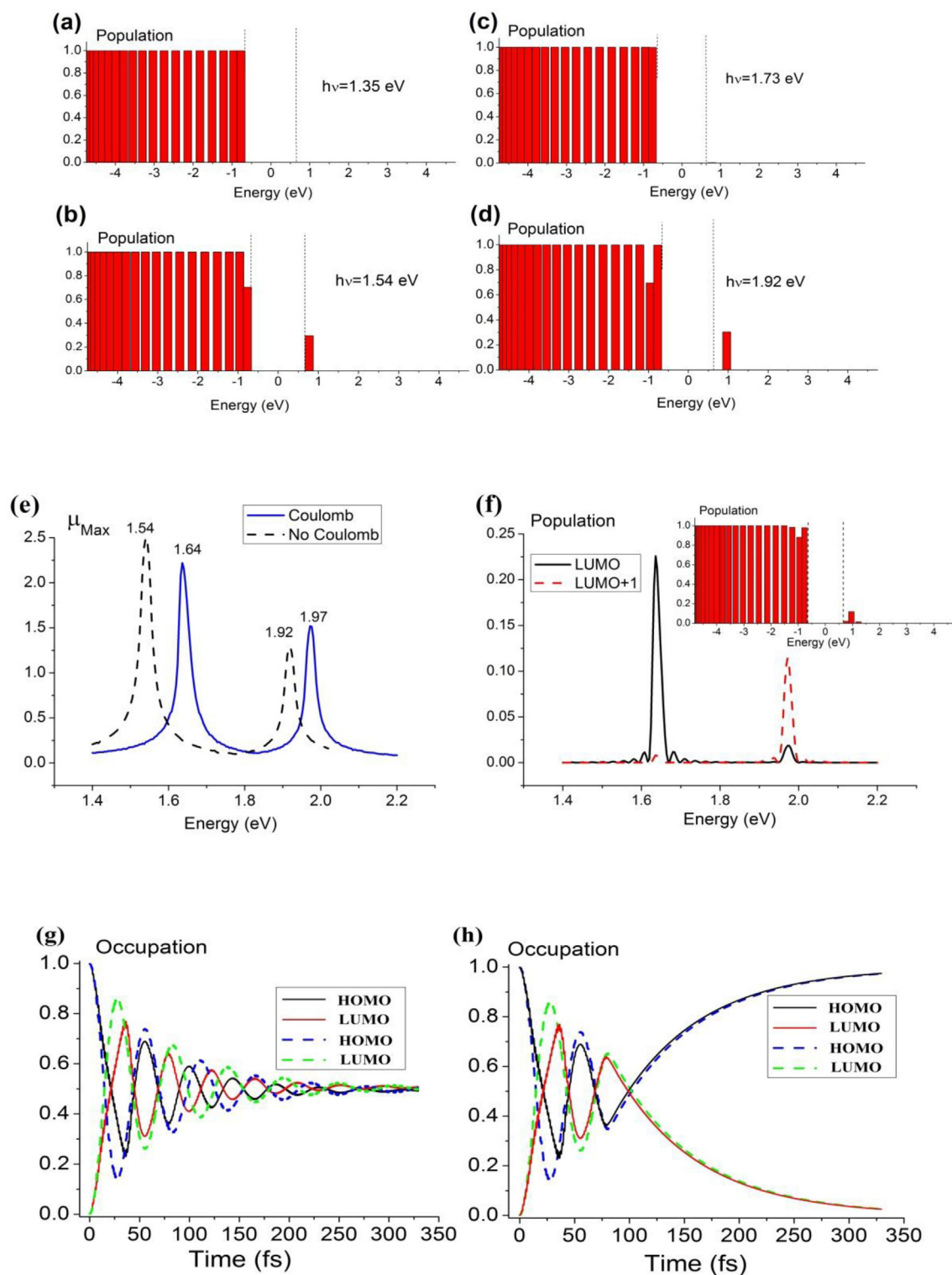


Fig. 2. The electron population on molecular orbitals for a short PA system ($N = 38$) under a spatial-uniform EM radiation. The electric potential of the light is 0.1 V. (a)–(d) show the orbital distribution under different EM frequencies: (a) $\hbar\omega = 1.35$ eV; (b) $\hbar\omega = 1.54$ eV; (c) $\hbar\omega = 1.73$ eV; (d) $\hbar\omega = 1.92$ eV. The two dashed lines in the figures indicate the edges of the valence and conduction bands. (e) shows the maximum dipole of this system under different frequencies of radiation with (blue solid line) and without (black dashed line) the Coulomb interaction. (f) shows the two molecular orbitals' populations (black solid line: LUMO mode; red dashed line: LUMO + 1 mode) under different frequencies of radiation. The inset is the population distribution at $\hbar\omega = 1.97$ eV. (g) and (h) show the two molecular orbitals' evolution under a constant EM radiation (see (g)) and a finite-time EM radiation (see (h)). The two solid lines correspond to the system with the Coulomb interaction and the two dashed lines correspond to the system without the Coulomb interaction. (For interpretation of the references to color in this figure legend, the reader is referred to the Web version of this article.)

$$\sigma_{i,j} = \sum_k^{occ} \phi_{ik}^* \phi_{jk} \quad (12)$$

Here the Hamiltonian \mathbf{H}_0 is for the finite chain system at time = 0 without any EPI. Then we use the equation of motion for the evolution of the density matrix

$$i\dot{\sigma}(t) = [\mathbf{H}_D(t), \sigma(t)]. \quad (13)$$

Finally a matrix transformation $\sigma_M = \mathbf{F}'\sigma\mathbf{F}$ is employed to obtain the orbital occupation for the electron. Here \mathbf{F} is the transformation matrix between the atomic orbital basis and the molecular orbital basis, which means $F_{i,j} = \phi_{i,j}$, where $\phi_{i,j}$ is from the eigenvalue calculation above.

Fig. 2(a)–(d) show the calculated molecular orbital population from the evolved electron density matrix at different excitation energy of EM wave. If a continuum-wave (cw) laser has the power about 8.2 W, and we assume the laser spot has the radius of 2 μm . According to the light intensity formula $I = \frac{1}{2}c\epsilon_0 E^2$, we can evaluate the electric field is 2.2×10^7 V/m, the EEP (V_m) along the PA chain is 0.12 eV. Now we calculate the EOM of electron density matrix by Eq. (13) with the Peierls factor for the EPI.

In Fig. 2 (a) we see that when the PA chain is illuminated by light with the energy smaller than the band-gap energy E_g (1.54 eV), there is almost no electron transition. When the energy of the illumination light (1.54eV) approaches or become a little larger than E_g , there are apparent transitions (Fig. 2(b)). The occupation of the HOMO orbital (with the energy $E_{-1} = -0.77$ eV) decreases to about 0.70; and the occupation of the LUMO orbital (with the energy $E_1 = 0.77$ eV) increase to about 0.30. In Fig. 2(c) when the illumination light has the energy of $E_2 - E_{-1}$ or $E_1 - E_{-2}$ (1.73 eV), there are no corresponding optical transition between these two levels. This is due to the selection rule for the dipole radiation [36]. In a PA system the orbitals have the similar forms as the eigenfunctions in a 1D infinite potential well. They have even or odd symmetry with the wavefunctions as $\phi_n(x) = \sin\left(\frac{n\pi x}{L}\right)$. So the transition matrix $\langle \phi_n | x | \phi_m \rangle$ gives the selection rule: only when $n-m$ is equal to an odd number, can the transition occur. Consequently, the transitions such as $E_2 \leftrightarrow E_{-1}$ or $E_1 \leftrightarrow E_{-2}$ are forbidden. In Fig. 2(d) the energy of illumination light is 1.92 eV, which is about the energy difference between E_{-2} and E_2 . We see there is an apparent transition since it obeys the selection rule.

In Figs. (a)–(d), we have not considered the Coulomb interaction, which means the system is a free-electron system. We now involve the Coulomb interaction in this radiation process. We introduce a dipole quantity (μ_{\max}) to represent the electron response under different frequencies of radiation. μ_{\max} is defined as the maximum value of the induced dipole

$$\mu_{\max} = \max \left[\sum_{i=1}^N \rho_i(t)(x_i - x_c), \quad 0 \leq t < T_0 \right]$$

where $\rho_i(t)$ and x_i is the electron density and x coordinate of the atom i ; x_c is the x coordinate of the system center; T_0 is the radiation time (160 fs). V_m along the PA chain is 0.06 eV. We find that with the Coulomb interaction, the resonance frequencies become larger than the free-electron case (Fig. 2(e)). For example, the $E_1 \leftrightarrow E_{-1}$ resonance transition energy is shifted from 1.54 eV to 1.64 eV. We explain this energy shift as a dynamic many-body interaction: With the Coulomb interaction, the non-equilibrium charge driven by the radiation E-field forms some a transient dipole. And the positive and negative parts of this dipole always have attraction Coulomb interaction. This Coulomb force has a superposition to the original ‘restoring force’ of the molecular system if we use the classical Lorentzian oscillator model to describe the light radiation on the solids [37]. Then from the basic resonance frequency relation: $f = \sqrt{K/m}$ (K is the force constant and m is the equivalent mass), we have $K = K_{\text{restoring}} + K_{\text{Coulomb}}$. In the interaction case, the force constant becomes larger, so the frequency also increases. We also draw the populations of two molecular orbitals (LUMO

and LUMO + 1) in difference driven frequencies, as shown in Fig. 2(f). We see that besides the previous resonance transition peaks, there exist some small peaks for the forbidden transitions of the two modes. The inset also shows this population distribution at $\hbar\omega = 1.97$ eV. We note that in this electron-electron interacting system, the eigenfunctions are not the original ones, so the transition matrix $\langle \phi_n | x | \phi_m \rangle$ will not lead to the previous selection rule. In other words, the rigid selection rule may be modified in the interaction system.

Furthermore, we use this basis transformation to investigate the orbital evolutions of an open system. The device is a PA chain with 38 carbon atoms sandwiched by two carbon chains (see Fig. 1(a)). We set a weak coupling between the device and the leads (with a hopping energy $t = -0.7$ eV). The molecular orbitals of the device (regarded as an isolate system due to the weak coupling) are calculated at first. Then the WBL-HEOM calculation is employed for the system under an EM radiation and the evolved density matrix is transformed to the molecular basis. A constant radiation (see Fig. 2 (g)) and a finite-period radiation (see Fig. 2 (h)), the radiation period ranges from 0 to 80 fs) are employed with the EM energy of 1.54 eV.

In Fig. 2(g), we see that the HOMO and LUMO orbitals oscillate and then tend to about 0.5. The oscillation amplitude decays with time like a damped Rabi model [38]. In this process the electrons transit mainly between HOMO and LUMO orbitals and exchange energies with the external EM wave. The decay is due to the dissipation source of two leads. This is different from the isolate system, in which the electrons will periodically transit between HOMO and LUMO orbitals as the Rabi cycle. In a long-time limit the generation and dissipation of these two orbitals reaches an equilibrium state. In the work of S. Latini and G. Stefanucci et al., similar occupation results are obtained by the Kadanoff-Baym equations (KBE) [19]. In Fig. 2(h) we see that after the EM radiation is turned off, the HOMO orbital occupation quickly goes back to 1 and the LUMO orbitals occupation goes back to 0. This is because the oscillation charges tend to dissipate into the two leads due to the spread of the waves and finally they return to the initial equilibrium state without radiation. We observe that in an isolate system all the occupations will become unchanged when turning off the radiation, because the inertial charge oscillations would not change the orbital occupations.

Here we also note that this dissipation is similar to the electron-hole recombination process: after the recombination, the electron in the conduction band (LUMO) returns to the valance band (HOMO). In general solar cells the recombination energy is taken away by phonons (the Shockley-Read-Hall process [9]); photons (radiative recombination due to the spontaneous emission [39]) or electrons (Auger recombination [40]). All these cases lead to the dissipation of the excited electrons and holes. In this PA system the dissipation is caused by the coupling of the leads, due to the spread nature of the electron waves.

At last, from Fig. 2(g) and (h) we see that when involving the Coulomb interaction, the population fluctuations (solid lines) becomes smaller than the non-Coulomb-interaction case (dashed lines). This is due to the electric attraction of opposite charges. As stated in Sec. 2.3, we consider the Coulomb interaction when there is some charge fluctuation beyond the equilibrium band structure of electron. In general, this Coulomb interaction plays an important role in a strong external field and in the dynamic process, as will be shown later.

And the electron-phonon interaction (EPI) also affects the transport properties of molecular devices [41,42]. We here assume that our system is in very low temperature, so EPI is not considered in this work.

Now we use our WBL-HEOM method to calculate the charges of a PA chain in real space. The PA chain, sandwiched by two carbon leads, is doped as n and p types which is the same as the case in photovoltaic devices. To obtain a large charge fluctuation, we use the pulse-typed laser with a high electric field. For example, a typical pulse with a duration time of 150 fs and the repeating frequency of 80 MHz from the Ti-sapphire laser is applied in the experiment. We assume the laser energy is about 0.1 nJ per pulse and the spot radius is 2 μm . With these

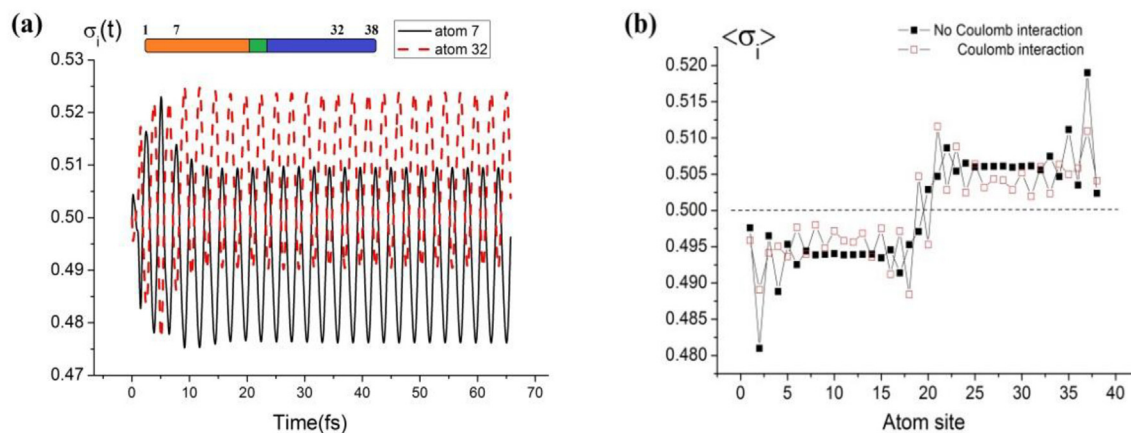


Fig. 3. The electron density situation of a PA chain under a uniform EM radiation with the radiation energy being $\hbar\omega = 1.55$ eV. (a) The electron density dependence on time in different atoms of a PA system (the black solid line is for atom 7 and the red dashed line is for atom 32); The inset shows the position of these two atoms in the PA chain (the yellow, blue and green colors denotes the p-doping, n-doping and the intrinsic regions). (b) The time-averaged electron density distribution on the PA chain. The filled-square line is without the Coulomb interaction; the empty-square line is with the Coulomb interaction. In (a) and (b), the PA has $N = 38$ atoms. The two bias potentials (± 0.2 eV) are applied on the two sides of PA chain. (For interpretation of the references to color in this figure legend, the reader is referred to the Web version of this article.)

conditions, the electric field can be evaluated as 2.0×10^8 V/m and the EEP (V_m) along the PA chain is 1.0 eV. In the WBL-HEOM simulation, EEP rises smoothly from the zero initial value to a sinusoidal function with the amplitude $V_m(t) = V_m(1 - e^{-t/\tau})\cos(\omega t)$.

Fig. 3 (a) shows several electron density variations versus time under a uniform EM radiation. The PA system (with 38 carbon atoms) has two bias potentials on the left and right regions (see Fig. 1(d)). We see the charge on the left side (in atom 7) oscillate with an average value below 0.5; and the charge on the right side (in atom 32) oscillate with an average value above 0.5. This is because that the positive bias potential on the left atoms leads to less electrons on them, while the negative bias potential on the right side attracts more electrons. Fig. 3(b) gives the average electron density distribution in the PA chain under the EM radiation with the energy of 1.55 eV (filled-square line) without considering the Coulomb interaction. For the same reason, we see the atoms in the left side almost have the lower electron populations than the atoms in the right side. If the Coulomb interaction is considered, the density (the empty-square line) deflection from the neutral density (0.5) becomes small due to the attraction between positive and negative fluctuation charges.

3.2. Charge separation in PA chains

Then we use a longer PA chain ($N = 160$) to study the dynamics of electron-hole separation. The EM pulse is radiated on the center region of the PA chain. As shown in Fig. 1(d)–(f), the radiation electric field is a Gaussian-typed pulse both in the time and spatial domain, $V_{ac}(x, t) = V_0(x)e^{-(t-t_0)^2/\tau^2}\cos(\omega t)$, where the spatial dependence of the electric field $V_0(x)$ is given as $V_0(x) = V_m e^{-(x-x_0)^2/A^2}$ for a pulse or $V_0(x) = V_m$ for a uniform EM wave. In our simulation, we set $t_0 = 6$ fs; $\tau = 2.5$ fs; $A = 4ax_0 = Na/2$. The energy of the EM wave is 2.5 eV. The laser energy is 7.8 nJ per pulse with 150 fs duration time and 80 MHz repeating frequency. The corresponding average power is 0.63 W and the equivalent electric potential along the PA chain is 40 V.

Fig. 4 (a)–(d) and (e)–(h) show four snaps of the averaged charge distribution at the time 4.0 fs, 8.0 fs, 13.2 fs and 18.5 fs. The PA chain has the uniform bias potential as shown in Fig. 1(d). The bias is set as $\Delta = \pm 0.4$ eV. In Fig. 4(a)–(d), the Coulomb interaction is not considered while in Fig. 4(e)–(h) the Coulomb interaction is involved. Due to the frequent charge fluctuations in time and space domain, some averaging implementation can be done to obtain the effective charge distribution. In this process, the electron charges on each atom are repeatedly averaged in a small period like one EM radiation period, in which the

transient fluctuations is eliminated and the intrinsic charge properties is revealed (similar to Fig. 3). If the averaged charge is negative, the atom is electron-like at that moment; and if the averaged value is positive, the atom is hole-like.

We see at the beginning the charge oscillations rise in the middle part of the PA chain. Then the oscillations tend to form the negative and positive fluctuation charge on the left and right side respectively. These two types of electron wave packet later move towards two sides with certain spread. At last these wave packets meet the device boundaries and dissipate into the two leads. There exist small reflection waves due to the mismatch between the device and the WBL leads. But this reflection is small so it can hardly be seen here. The same profile of wave packets for the electron and hole is due to the symmetry of the conduction/valence bands in the tight-binding model. It is noticed that the Coulomb interaction makes the charge fluctuation much smaller but more frequent in space, and the wave packets in Fig. 4(e)–(h) have a wider spread. This wide spread makes a slower separation speed (group velocity) compared to the case without the Coulomb interaction. From these figures we estimate the charge separation speed in the PA chain ranging from about 0.2×10^6 m/s to 0.6×10^6 m/s, which is comparable to the simulation results in silicon nanowire in low radiation intensity by the classical drift-diffusion model [7].

As a comparison, we calculate for the carrier dynamics in the PA chain without any bias or dopant (Fig. 4(i)–(l)). Since there is no bias potential, the excited charge fluctuations have no net positive/negative profiles as before and the averaged charge distribution (blue curve) is smaller. We also plot the averaged fluctuation amplitude profile (red curve) for this system. The amplitude profile reflects the whole charge fluctuations, and its calculation details will be demonstrated in Fig. 6 later.

Similarly, we also use the WBL-HEOM scheme to calculate for the charge separation process for a PA chain with two types of separate doping atoms. The doping atoms have positive or negative on-site potentials ($\Delta = \pm 2.0$ eV) and are separated by the same number of carbon atoms on the two sides (see Fig. 1(e)). The EM radiation and other parameters are the same as in the previous case. Fig. 5 (a) shows two snaps of fluctuation charge with the doping atoms in every 4 carbon atoms. Fig. 5 (b) shows the similar snaps with the doping in every 10 atoms. We see that the electron-hole wave packets in these two cases almost have the similar profiles and the charge fluctuation in the low doping concentration (every 10 atoms) is smaller.

Now we investigate the electron-hole separation speed under different illumination intensities. When increasing the light intensity (or

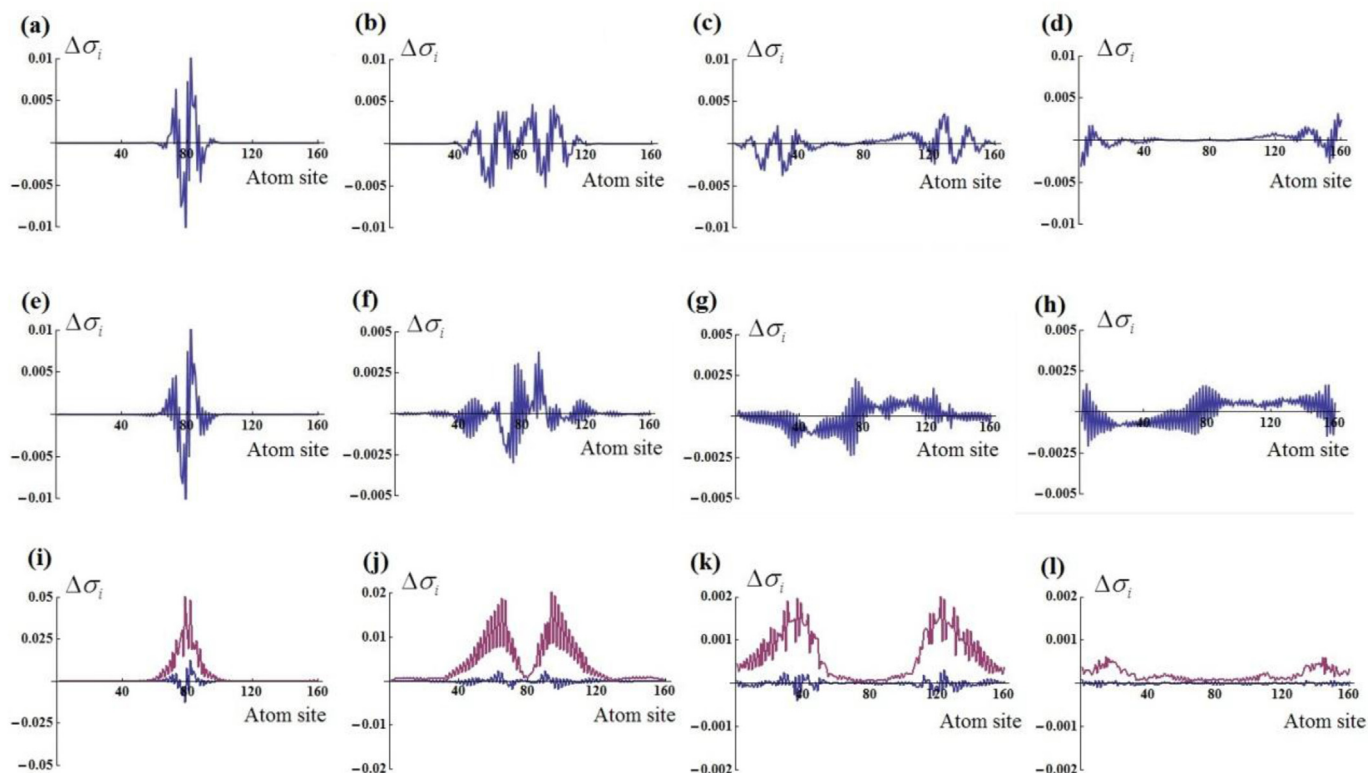


Fig. 4. Snaps of the charge evolution in the PA system ($N = 160$) under a EM pulse ($\hbar\omega = 2.5$ eV) radiated in the middle region of the system. In the (a)–(d) (upper panel) no Coulomb interaction is considered; while in (e)–(h) (middle panel) and (i)–(l) (lower panel), Coulomb interaction is considered. In the upper and middle panels the bias potentials ($\Delta = \pm 0.4$ eV) are applied on the two sides and in the lower panel there is no bias potential. In the lower panel the red curves denote the fluctuation envelopes. In these three panels, the snap is taken at time = 4.0 fs; 8.0 fs; 13.2 fs; 18.5 fs respectively. (For interpretation of the references to color in this figure legend, the reader is referred to the Web version of this article.)

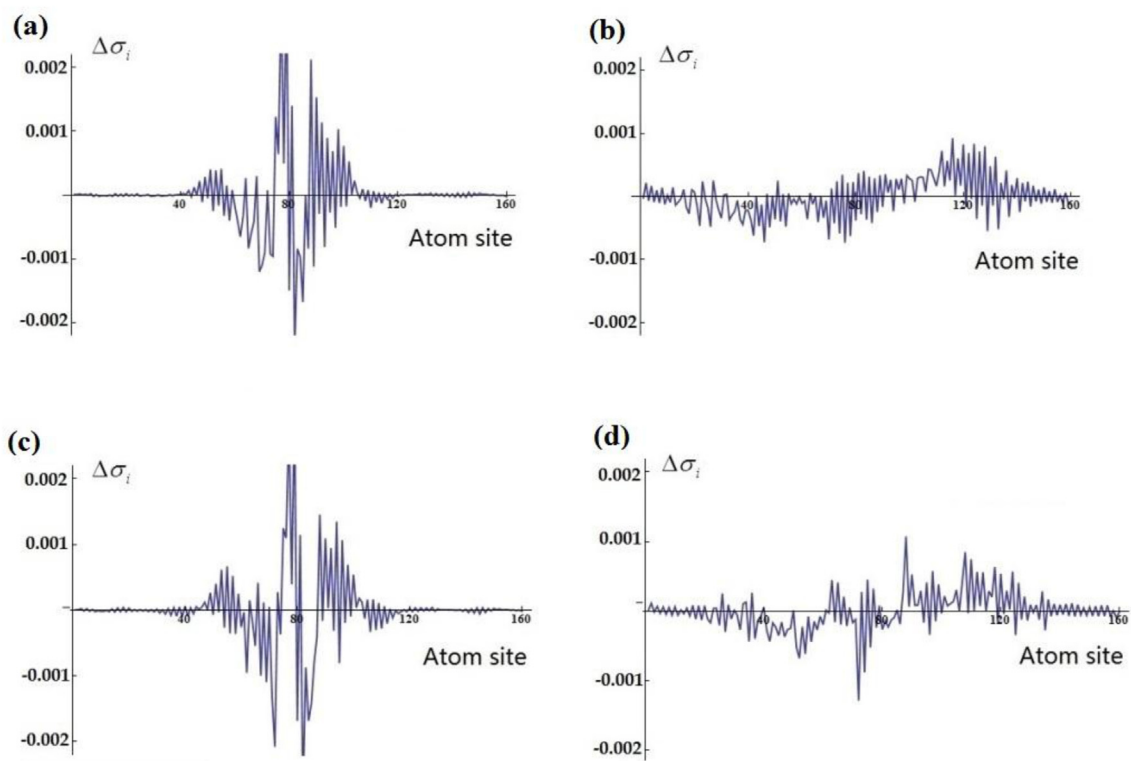


Fig. 5. Snaps of the electron and hole evolution in the PA system ($N = 160$) under a EM pulse ($\hbar\omega = 2.5$ eV) radiated in the middle region of the system. The snap time is 6.6 fs ((a),(c)) and 14.6 fs ((b),(d)). In (a) and (b), the impurity atoms locate in every 4 sites with the potentials: $\Delta = \pm 2.0$ eV in the left and right parts; In (c) and (d) the impurity atoms locate in every 10 sites with the potentials: $\Delta = \pm 2.0$ eV in the left and right parts.

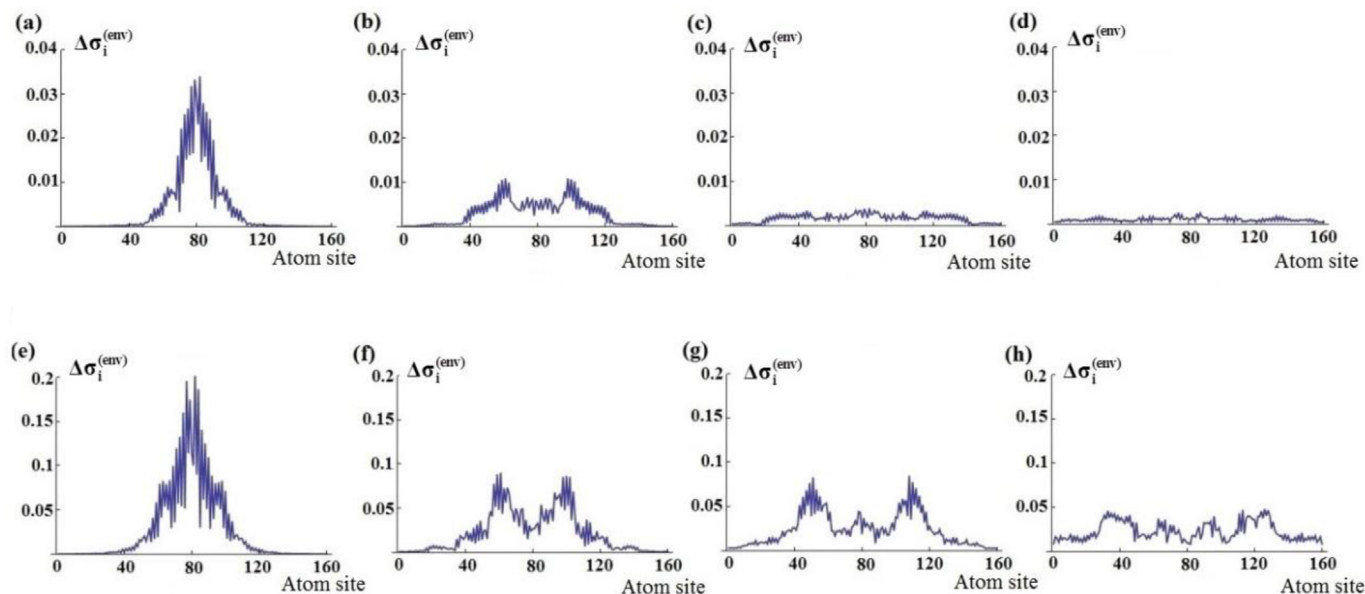


Fig. 6. The charge spread dynamics under a weak laser light (upper panel, with 7.8 nJ per pulse or EEP = 40 eV) and strong laser light (lower panel, with 12.5 μJ per pulse or EEP = 1600 eV) in a p-i-n typed PA chain ($N = 160$, with the averaged impurity potentials: $\Delta = \pm 0.4$ eV). In the upper panel the snaps of charge envelopes at 5.3 fs (a); 7.9 fs (b); 10.5 fs (c) and 13.2 fs (d) are shown. In the lower panel, the snaps of charge envelopes at 5.3 fs (e); 7.9 fs (f); 10.5 fs (g) and 13.2 fs (h) are shown.

the excitation electric potential), the charge fluctuation becomes larger. Due to the Coulomb attraction between the electrons and holes, we expect that the wave packets under a strong light intensity will spread slower than those in a weak light condition [7]. However, we find that the previous average processing scheme is not suitable here. This is because the fluctuation effect is eliminated by the averaging process. In this case different charge fluctuations by the radiations also reflect the wave packet speed. To observe the wave packet evolution clearly, we draw the envelope lines of the wave packet by taking out the maximum amplitude of charge on each atom during one EM period, like the formula below

$$\Delta\sigma_i^{(env)}(\bar{t}) = \max[|\Delta\sigma_i(t)|, \quad n\tau \leq t < (n+1)\tau].$$

In this formula, the superscript (env) means the envelope; τ is the EM wave period; $\bar{t} = n\tau$ is the coarse time for the enveloped charge during one EM period. It is noted that only the absolute value is used here for the amplitude of fluctuated charges. We do not concern the signs (electron/hole) of $\Delta\sigma_i$ in this case.

Fig. 6 shows such results for the weak and strong light cases. It is easy to see that under a strong light illumination (Fig. 6(e)–(h)), the large charge fluctuation occurs and the Coulomb interaction make a slower separation speed for the wave packets, compared to the envelope lines under a weak light illumination (Fig. 6(a)–(d)).

This is similar to the classical simulation and the experimental measurements for silicon nanowires [7]. In the semi-classical drift-diffusion model, the electrons and holes move driven by the electric field (drift part) and the concentration gradient (diffusion part). The electric field is determined from the Poisson equation which is determined by the total charges and external voltages. Hence, the large fluctuated charge leads to a large Coulomb attraction, which makes a slow separation for the two opposite charge distributions in the nanowire [7]. Our calculation is about the ballistic motion for the coherent electrons. The device size is smaller than the phase-relaxation path, so the electron-phonon scattering and electron-electron interaction is reduced, resulting in a fast wavepacket spread [43]. In this quantum regime, the kinetic motion of the wave packets plays a major role. Only when the Coulomb interaction energies are comparable to the hopping (kinetic) energies, the Coulomb-related charge separation reduction can occur. This explains a very large charge fluctuation (about 0.1–0.2 in

Fig. 6(e)–(h)) is needed for the electron-hole localization under a strong light.

3.3. Charge separation in PP and doped PP systems

In the last section, we apply this WBL-HEOM method to PP systems for investigating the charge separation. The PP chain consists of 60 benzene units as shown in Fig. 1(b). A bias potential of ± 0.2 eV is applied on the two sides to stand for the n-doping and p-doping regions. For the laser, the energy ($\hbar\omega$) is 2.7 eV and EEP (V_m) is 8.0 eV. Other parameters about the pulse are as same as before. Similar to Figs. 4 and 5, a short-time-average scheme is used to show the electron-hole evolutions in the PP chain. In Fig. 7 we see an apparent positive and negative charge separation and movement towards the two sides after a pulse is radiated in the middle of the chain. After some time about 20 fs, the separated charges reach the lead regions and dissipated out. The involvement of the Coulomb interaction also makes the spread of the two wave packets.

Finally, we choose another PP chain system doped with boron and nitrogen atoms as described in Fig. 1(c). We design a heterocyclic ring as the unit of a molecular wire. In each unit three heterogeneous atoms (one boron and two nitrogen atoms) are doped in one benzene ring. We notice that some B/N-doped graphene junction can also be used as the molecular rectifying device [29].

The DFTB method is employed for the band structure. DFTB is an approximation of density-functional-theory (DFT) model derived from the second-order expansion of Kohn-Sham energy around the reference charge density [30–32]. A free software package: DFTB+ [30,31] developed by the Th. Frauenheim's group is used in our paper. The vacuum layers of 40 nm in the ribbon plane and 50 nm in the normal direction is applied to avoid the interaction between ribbons in different unit cells. In the SCC iteration we choose the Broyden mixing scheme and the energy tolerance is set to 1×10^{-6} eV. The geometric structure of the unit cell is optimized by the conjugate gradient algorithm with the Brillouin zone sampling of 100 points in x direction.

Fig. 8(a) shows the DFTB band structure. We see that there exist an energy gap of 2.2 eV and the valence band curvature at $k = 0$ is found to be larger than the conduction band curvature (with a ratio of 1.1). This means that the effective mass of hole in the valence band is smaller

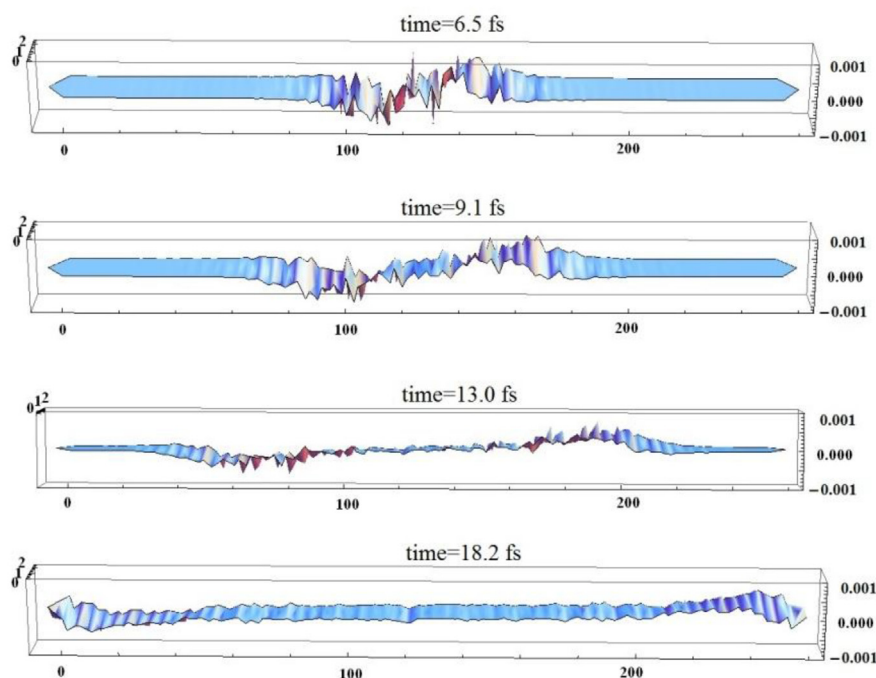


Fig. 7. Snaps of the charge separation process in the PP chain (60 benzene units) under a laser pulse illuminated in the middle. The bias potentials on the two sides of PP chain is ± 0.2 eV and the EEP of the EM radiation is 8.0 eV.

than that of electron in the conduction band. To calculate the dynamic process with our WBL-HEOM method, a TB model is needed. With some suitable parameters similar to the previous studies [44,45], we obtain the band structure by the TB model (Fig. 8(b)). In this effective TB model we only change the on-site energies of carbon/boron/nitrogen atoms (we change the on-site energies of B and N atoms as $\varepsilon_B = \varepsilon_3 = 3.70$ eV; $\varepsilon_N = \varepsilon_1 = \varepsilon_6 = -0.85$ eV; the on-site energies of other C atoms are evaluated from all the contributions of the neighboring B/N atoms with decaying trends as shown in Fig. 3 of reference [44]: $\varepsilon_2 = 0.90$ eV; $\varepsilon_4 = 1.46$ eV; $\varepsilon_5 = 1.56$ eV). Both bands are shifted

to zero as its Fermi level. We see these two bands have some differences. However the basic band properties near the Fermi level remain the same: the TB band has a gap of 2.0 eV and the curvature of the valence band is larger than that of the conduction band (with a ratio of 1.2). Although the band gap and curvature ratio are a little larger than the DFTB values, we believe this TB model may effectively mimic the basic optical excitations for this heterocyclic system.

Similar to the setup in Fig. 7, we apply the uniform potentials (± 0.2 eV) on the left and right parts of the molecular chain for mimicking the p-type and n-type doping. Then a laser pulse with an

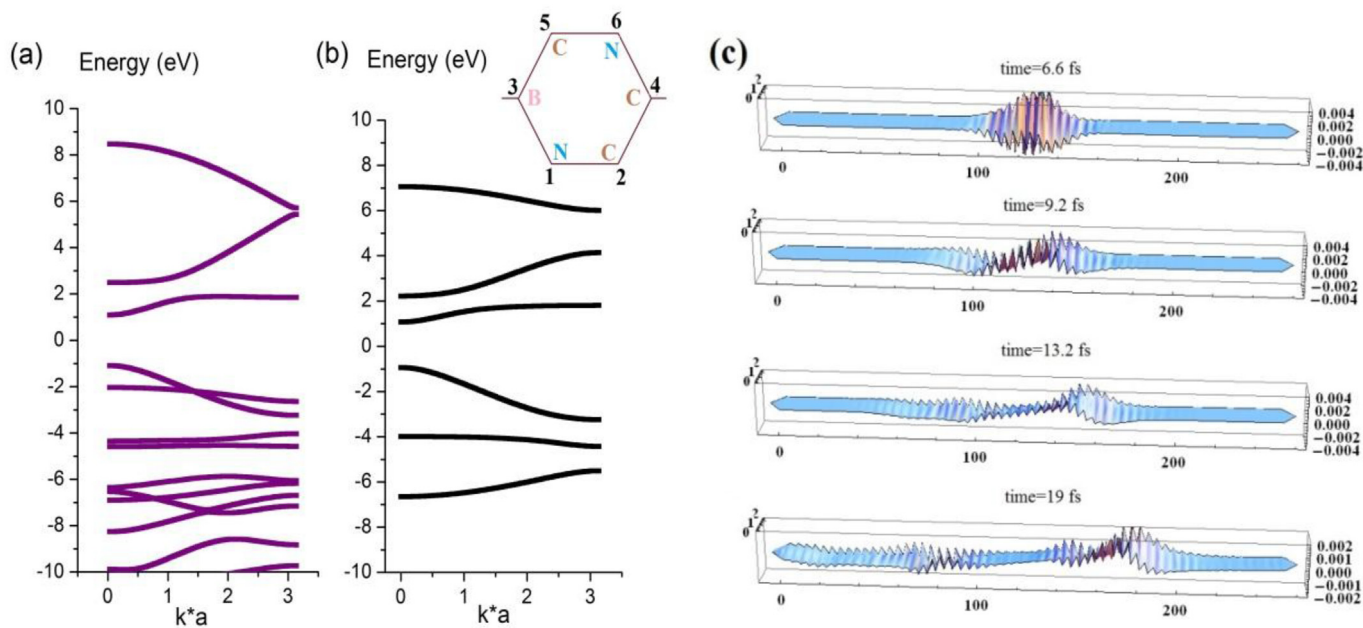


Fig. 8. DFTB (a) and TB (b) band structures of the boron-and-nitrogen-doped PP system (60 heterocyclic ring units). The detailed atomic structure of the doped PP is shown in Fig. 1(c). The inset figure shows the atom indexes of a heterocyclic ring in the TB model. (c) Dynamic electron and hole separation processes in this doped PP chain under a laser pulse with the energy of 2.1 eV and EEP of 16 eV.

energy of 2.1 eV and EEP of 16 eV is radiated on the middle of the system. The snaps with some time average are shown in Fig. 8(c). It is apparent to see that the negative wavepacket (corresponding to excited holes in valence band) has a much quicker separation than the positive wavepacket (corresponding to excited electrons in conduction band). This is expected as a result of a larger effective mass for the electron. And the hole-type wavepacket is found to have a much larger spread behavior in this dynamic process. There are similar observations and simulations in the previous works in silicon nanowire [7,8].

4. Conclusions

The time-dependent quantum transport method is employed to molecular wire systems for investigating the dynamic charge dissipation and separation behaviors. The method is based on the HEOM theory with the wide-band-limit approximation. The Coulomb interaction is considered by the spin-unpolarized Hubbard model.

For a finite PA chain under a uniform EM radiation, only the transitions obeying the selection rules can occur for the free-electron model. With the Coulomb interaction, the resonance transition energy becomes larger due to the additional electric attraction forces. For an open PA system with a weak-coupling, the electrons in the valence band are excited to the conduction bands by the radiation with a damped oscillation. When turning off the radiation, the electrons in the conduction band smoothly return to valence band due to the dissipation of the leads. The Coulomb interaction makes smaller orbital fluctuations during these dynamic processes.

The wavepacket evolution in the PA and PP chains is calculated with the atom-doping or bias potential condition under a pulse laser. In PA chains, we find the electron-type and hole-type wavepackets have the same separation behaviors. The Coulomb interaction involution leads to small and frequent fluctuations with wide spreads. In a strong illumination, the wave packet profile has a slower separation speed. The typical separation speed is from about 0.2×10^6 m/s to 0.6×10^6 m/s. In PP systems, we find similar charge separation behaviors. In the doped PP chain with the empirical TB Hamiltonian, we find the hole-type wavepacket moves faster than the electron-type wavepacket due to their asymmetric effective masses.

Therefore, in the molecular wires, we observe the dynamic orbital transition and carrier dissipation in the mode space, and the charge separation dynamics in the real space. We believe this HEOM-WBL method is a good tool to study the complex quantum dynamics of carriers under a photon radiation in open nano devices. This study is useful to analyze the microscopic mechanism of photovoltaics in the quantum regime. Some potential factors such as electron-phonon interaction and radiative recombination may be involved in the future researches.

Acknowledgement

The authors are grateful to Prof. Guanhua Chen in the University of Hong Kong for useful discussions and help. We thank Dr. Yong Wang in Nankai University for the helpful discussions on the exciton theory, and Dr. Rui Wang in the Chongqing University for the kind help of the computer service. Financial support from the starting foundation of Chongqing University (Grants No. 0233001104429) is also gratefully acknowledged.

References

- [1] T.J. Kempa, B. Tian, D.R. Kim, J. Hu, X. Zheng, C.M. Lieber, Single and tandem axial p-i-n nanowire photovoltaic devices, *Nano Lett.* 8 (2008) 3456–3460.
- [2] Z.F. Liu, Q. Liu, Y. Huang, Y.F. Ma, S.G. Yin, X.Y. Zhang, W. Sun, Y.S. Chen, Organic photovoltaic devices based on a novel acceptor material: graphene, *Adv. Mater.* 20 (2008) 3924.
- [3] Z.G. Song, Z.W. Lips, H. Wang, X.D. Bai, W.L. Wang, H.L. Du, S.Q. Liu, C.S. Wang, J.Z. Han, Y.C. Yang, Z. Liu, J. Lu, Z.Y. Fang, J.B. Yang, Valley pseudospin with a widely tunable bandgap in doped honeycomb BN monolayer, *Nano Lett.* 17 (2017) 2079–2087.
- [4] Y. Lu, J. Guo, Band gap of strained graphene nanoribbons, *Nano Research* 3 (2010) 189–199.
- [5] Z.G. Wu, J.B. Neaton, J.C. Grossman, Charge separation via strain in silicon nanowires, *Nano Lett.* 9 (2009) 2418–2422.
- [6] E.M. Grumstrup, M.M. Gabriel, C.W. Pinion, J.K. Parker, J.F. Cahoon, J.M. Papanikolas, Reversible strain-induced electron-hole recombination in silicon nanowires observed with femtosecond pump-probe microscopy, *Nano Lett.* 14 (2014) 6287–6292.
- [7] M.M. Gabriel, E.M. Grumstrup, J.R. Kirschbrown, C.W. Pinion, J.D. Christesen, D.F. Zigler, E.E.M. Cating, J.F. Cahoon, J.M. Papanikolas, Imaging charge separation and Carrier recombination in nanowire p-i-n junctions using ultrafast microscopy, *Nano Lett.* 14 (2014) 3079–3087.
- [8] M.M. Gabriel, J.R. Kirschbrown, J.D. Christesen, C.W. Pinion, D.F. Zigler, E.M. Grumstrup, B.P. Mehl, E.E.M. Cating, J.F. Cahoon, J.M. Papanikolas, Direct imaging of free Carrier and trap Carrier motion in silicon nanowires by spatially-separated femtosecond pump-probe microscopy, *Nano Lett.* 13 (2013) 1336–1340.
- [9] J.D. Christesen, X. Zhang, C.W. Pinion, T.A. Celano, C.J. Flynn, J.F. Cahoon, Design principles for photovoltaic devices based on Si nanowires with axial or radial p-n junctions, *Nano Lett.* 12 (2012) 6024–6029.
- [10] Z.S. Wang, W.E.I. Sha, W.C.H. Choy, Exciton delocalization incorporated drift-diffusion model for bulk-heterojunction organic solar cells, *J. Appl. Phys.* 120 (2016) 213101.
- [11] W.E.I. Sha, W.C.H. Choy, Y.M. Wu, W.C. Chew, Optical and electrical study of organic solar cells with a 2D grating anode, *Optic Express* 20 (2012) 2572–2580.
- [12] E.E. Salpeter, H.A. Bethe, A relativistic equation for bound-state problems, *Phys. Rev.* 84 (1951) 1232–1242.
- [13] J.W. van der Horst, P.A. Bobbert, P.H.L. de Jong, M.A.J. Michels, G. Brocks, P.J. Kelly, Ab initio prediction of the electronic and optical excitations in polythiophene: isolated chains versus bulk polymer, *Phys. Rev. B* 61 (2000) 15817–15826.
- [14] L.X. Benedict, E.L. Shirley, Ab initio calculation of $\epsilon(2)/\omega$ including the electron-hole interaction: application to GaN and CaF₂, *Phys. Rev. B* 59 (1999) 5441–5451.
- [15] D. Shiri, Y. Kong, A. Buin, M.P. Anantram, Strain induced change of bandgap and effective mass in silicon nanowires, *Appl. Phys. Lett.* 93 (2008) 073114.
- [16] D. Shiri, A. Verma, C.R. Selvakumar, M.P. Anantram, Reversible modulation of spontaneous emission by strain in silicon nanowires, *Sci. Rep.-Uk* 2 (2012) 461.
- [17] Y. Zhang, L.Y. Meng, C. Yam, G.H. Chen, Quantum-mechanical prediction of nanoscale photovoltaics, *J. Phys. Chem. Lett.* 5 (2014) 1272–1277.
- [18] J.Z. Chen, Y.B. Hu, H. Guo, First-principles analysis of photocurrent in graphene PN junctions, *Phys. Rev. B* 85 (2012) 155441.
- [19] S. Latini, E. Perfetto, A.M. Uimonen, R. van Leeuwen, G. Stefanucci, Charge dynamics in molecular junctions: nonequilibrium Green's function approach made fast, *Phys. Rev. B* 89 (2014) 075306.
- [20] E.A. Weiss, M.J. Ahrens, L.E. Sinks, A.V. Gusev, M.A. Ratner, M.R. Wasielewski, Making a molecular wire: charge and spin transport through para-phenylene oligomers, *J. Am. Chem. Soc.* 126 (2004) 5577–5584.
- [21] J.J.M. Halls, J. Cornil, D.A. dos Santos, R. Silbey, D.H. Hwang, A.B. Holmes, J.L. Bredas, R.H. Friend, Charge- and energy-transfer processes at polymer/polymer interfaces: a joint experimental and theoretical study, *Phys. Rev. B* 60 (1999) 5721–5727.
- [22] Y. Zhang, S.G. Chen, G.H. Chen, First-principles time-dependent quantum transport theory, *Phys. Rev. B* 87 (2013) 085110.
- [23] H. Xie, Y. Kwok, Y. Zhang, F. Jiang, X. Zheng, Y.J. Yan, G.H. Chen, Time-dependent quantum transport theory and its applications to graphene nanoribbons, *Phys. Status Solidi B* 250 (2013) 2481–2494.
- [24] H. Xie, F. Jiang, H. Tian, X. Zheng, Y. Kwok, S.G. Chen, C. Yam, Y.J. Yan, G.H. Chen, Time-dependent quantum transport: an efficient method based on Liouville-von-Neumann equation for single-electron density matrix, *J. Chem. Phys.* 137 (2012) 044113.
- [25] H. Xie, Y. Kwok, F. Jiang, X. Zheng, G.H. Chen, Complex absorbing potential based Lorentzian fitting scheme and time dependent quantum transport, *J. Chem. Phys.* 141 (2014) 164122.
- [26] R.E. Thorne, Charge-density-wave conductors, *Phys. Today* 49 (1996) 42–47.
- [27] Z.Q. Fan, Z.H. Zhang, W. Tian, X.Q. Deng, G.P. Tang, F. Xie, Altering regularities on resistances of doped Au-alkanedithiol-Au junctions, *Org. Electron.* 14 (2013) 2705–2710.
- [28] B. Jiang, Y.H. Zhou, C.Y. Chen, K.Q. Chen, Designing multi-functional devices based on two benzene rings molecule modulated with Co and N atoms, *Org. Electron.* 23 (2015) 133–137.
- [29] Y.C. Ling, F. Ning, Y.H. Zhou, K.Q. Chen, Rectifying behavior and negative differential resistance in triangular graphene p-n junctions induced by vertex B-N mixture doping, *Org. Electron.* 19 (2015) 92–97.
- [30] M. Elstner, D. Porezag, G. Jungnickel, J. Elsner, M. Haugk, T. Frauenheim, S. Suhai, G. Seifert, Self-consistent-charge density-functional tight-binding method for simulations of complex materials properties, *Phys. Rev. B* 58 (1998) 7260–7268.
- [31] M. Wahiduzzaman, A.F. Oliveira, P. Philippsen, L. Zhechkov, E. van Lenthe, H.A. Witek, T. Heine, DFTB parameters for the periodic table: Part 1, electronic structure, *J. Chem. Theor. Comput.* 9 (2013) 4006–4017.
- [32] Y. Wang, C.Y. Yam, T. Frauenheim, G.H. Chen, T.A. Niehaus, An efficient method for quantum transport simulations in the time domain, *Chem. Phys.* 391 (2011) 69–77.
- [33] C.C. Wan, P. Sheng, Quantum interference and the giant Hall effect in percolating systems, *Phys. Rev. B* 66 (2002) 075309.

- [34] M. Graf, P. Vogl, Electromagnetic-fields and dielectric response in empirical tight-binding theory, *Phys. Rev. B* 51 (1995) 4940–4949.
- [35] A. Szabo, N.S. Ostlund, *Modern quantum chemistry : introduction to advanced electronic structure theory*, McGraw-Hill Publishing Company, 1989, pp. 136–139 Sec.3.4.
- [36] J.J. Sakurai, S.F. Tuan, E.D. Commins, *Modern quantum mechanics, revised edition*, *Am. J. Phys.* 63 (1995) 93–95.
- [37] M. Fox, *Optical Properties of Solids*, Oxford University Press, 2001.
- [38] D.P.S. McCutcheon, N.S. Dattani, E.M. Gauger, B.W. Lovett, A. Nazir, A general approach to quantum dynamics using a variational master equation: application to phonon-damped Rabi rotations in quantum dots, *Phys. Rev. B* 84 (2011) 081305.
- [39] M.O. Scully, Quantum photocell: using quantum coherence to reduce radiative recombination and increase efficiency, *Phys. Rev. Lett.* 104 (2010) 207701.
- [40] J. Iveland, L. Martinelli, J. Peretti, J.S. Speck, C. Weisbuch, Direct measurement of Auger electrons emitted from a semiconductor light-emitting diode under electrical injection: identification of the dominant mechanism for efficiency droop, *Phys. Rev. Lett.* 110 (2013) 177406.
- [41] B.L. Li, K.Q. Chen, Huge inelastic current at low temperature in graphene nanoribbons, *J Phys-Condens Mat* 29 (2017) 075301.
- [42] Y.Y. Liu, B.L. Li, S.Z. Chen, X.W. Jiang, K.Q. Chen, Effect of room temperature lattice vibration on the electron transport in graphene nanoribbons, *Appl. Phys. Lett.* 111 (2017) 133107.
- [43] S. Datta, *Electronic Transport in Mesoscopic Systems*, Cambridge University Press, U.K, 1995.
- [44] C. Adessi, S. Roche, X. Blase, Reduced backscattering in potassium-doped nanotubes: ab initio and semiempirical simulations, *Phys. Rev. B* 73 (2006) 125414.
- [45] M. Modarresi, M.R. Roknabadi, N. Shahtahmasbi, Transport properties of an arm-chair boron-nitride nanoribbon embedded between two graphene electrodes, *Physica* 43 (2011) 1751–1754.